Journal of Geophysical Research: Space Physics

RESEARCH ARTICLE
10.1029/2018JA025705

Evolution of Freshly Generated Equatorial Spread F (F-ESF) Irregularities on Quiet and Disturbed Days

P. Gurram[1], B. Kakad[1], A. Bhattacharyya[1], and T. K. Pant[2]

[1]Indian Institute of Geomagnetism, Navi Mumbai, India, [2]Space Physics Laboratory, Vikram Sarabhai Space Centre, Trivandrum, India

Key Points:
- Perturbation electric field linked with fresh ESF is sustained for longer duration on disturbed days
- Disturbed time fresh ESF irregularities produce stronger scintillations as compared to quiet time fresh ESF
- Theoretical model indicates a smaller altitudinal extent for postmidnight fresh ESF on quiet days as compared to disturbed days

Correspondence to:
P. Gurram,
padmagurram123@gmail.com

Citation:
Gurram, P., Kakad, B., Bhattacharyya, A., & Pant, T. K. (2018). Evolution of freshly generated equatorial spread F (F-ESF) irregularities on quiet and disturbed days. *Journal of Geophysical Research: Space Physics*, *123*, 7710–7725. https://doi.org/10.1029/2018JA025705

Received 23 MAY 2018
Accepted 14 AUG 2018
Accepted article online 29 AUG 2018
Published online 10 SEP 2018

Abstract We examined the seasonal and solar flux dependence of the occurrence of freshly generated intermediate scale (100 m to few km) equatorial spread F (ESF) irregularities during magnetically quiet (Q) and disturbed (D) periods. We utilized long-term (1992–2006 and 2013–2015) amplitude scintillation data on a 251 MHz signal recorded at Tirunelveli (dip lat. 1.5°N). Also, ionosonde data (1990–2003) recorded at Trivandrum (dip lat. 0.5°N) are used. The presence of fresh ESF (F-ESF) is identified using the maximum cross-correlation between intensity variations recorded by two spaced receivers on a magnetic east-west baseline. We find distinct differences in the seasonal and solar flux dependence of the usual postsunset (<22 LT) generation of F-ESF on both Q- and D-days. Interesting feature is that F-ESF linked moderate–strong scintillations are more prevalent on D-days as compared to Q-days in both early (18–22 LT) and later (>22 LT) phase of evolution of the irregularities. It directly hints toward the difference in the spatial structuring (spatial scales) of F-ESF on D-days as compared to Q-days. On D-days, the occurrence of F-ESF is more likely around midnight and early-morning hours in all seasons. Whereas on Q-days, the postmidnight F-ESF is found to occur mainly during solstices of low solar activity. The possible sources for the generation of F-ESF around midnight on Q-days of solstices during low solar activity are examined. We also find that perturbation electric field linked with F-ESF on D-days sustains for longer time, which results in longer durations of the active phase of equatorial plasma bubbles.

1. Introduction

In the postsunset hours, equatorial ionospheric F-region moves to higher altitude through the mechanism called as prereversal enhancement (PRE), where usual daytime eastward electric field is enhanced before turning westward. At this time, both decrease in ionization due to cutoff of solar radiation and dissociative recombination results in sharp vertical density gradients at the bottomside of F-region. These are favorable conditions for the growth of Rayleigh Taylor (RT) plasma instability, which leads to the formation of electron density irregularities referred to equatorial spread F (ESF). Other secondary instabilities grow on these large-scale structures to give rise to small scale irregularities. As a consequence, the ESF irregularities cover a broad spectrum starting from hundreds of kilometers down to few centimeters. Although these ambient favorable conditions are present everyday in the postsunset hours, the generation of ESF irregularities is not seen on every day due to variation in amplitudes and scale size of the seed perturbation (Sekar et al., 1995). Such seed or triggering perturbations are sometimes provided by gravity waves (Hysell et al., 1990; Krall et al., 2013), by spatially varying electric fields (C.-S. Huang & Kelley, 1996), or by large-scale wave structures on the bottomside of F-region (Joshi et al., 2015; Tsunoda, 2012). A radio wave signal undergoes phase and amplitude scintillations while traversing through such irregular medium of varying refractive index (Yeh & Liu, 1982). Sometimes, a VHF signal can be completely degraded due to the presence of fast moving intermediate scale (100 m to few km) irregularities. Hence, information of characteristics of ESF irregularities is crucial for radio communication and navigation systems.

Equatorial plasma bubbles (EPBs) and dynamics of associated ESF irregularities of different spatial scales are being studied for the last few decades. But its study still forms an important element of ionospheric research due to the uncertainties involved in the day-to-day prediction of occurrence of these EPBs. Several studies have demonstrated that parameters like postsunset height of F-layer, ambient eastward electric field, ambient magnetic field, horizontal conductivity gradients in the E-region, vertical density gradient at the bottomside of F-region, neutral wind speed, ion-neural collision frequency, and alignment of sunset terminator with mag-

netic meridian play an important role in the generation of the ESF irregularities (Abdu et al., 2008; Basu et al., 1996; Bhattacharyya, 2004; Patra et al., 1997; Tsunoda, 1985). Climatological models for the ionospheric zonal and vertical plasma drifts were proposed using Jicamarca radar observations (Fejer et al., 2008), which provides information about the equatorial electric field. The occurrence of the EPBs varies with solar flux, seasons, geomagnetic activity, longitude, and latitude (Burke et al., 2004; Nishioka et al., 2008; Sahai et al., 2000; J. Smith & Heelis, 2017). Li et al. (2008) have shown that vertical ($\mathbf{E} \times \mathbf{B}$) drift associated with PRE is likely to be responsible for the global large-scale variations in the longitudinal distribution of evening equatorial ionospheric anomaly enhancement and plasma bubbles occurrence rates. Studies have demonstrated that on disturbed (D) days, a disturbance dynamo (DD) electric field (Blanc & Richmond, 1980), promptly penetrated (PP) electric field (Kikuchi et al., 2000, 2008), or combination of DD and PP electric fields affects the dynamics of F-region (Kakad et al., 2011; N. Maruyama et al., 2005). Apart from usual postsunset generation, fresh development of EPBs is often encountered in the postmidnight hours on the D-days (Kakad et al., 2007). The seasonal and solar flux dependence of these magnetic activity linked F-EPBs is not studied so far. There are reports of midnight EPBs even on quiet (Q) days particularly during summer solstice of low solar activity period (Ajith et al., 2016; Chakrabarty et al., 2014; Niranjan et al., 2003), but the mechanism responsible for their generation needs further in-depth understanding.

For Q- and D-days, we are not only interested in the occurrence EPBs but we are also keen to know the level of degradation caused to incoming radio signal by these F-EPBs, which is closely related to the strength and spatial scales of the ESF irregularities (Bhattacharyya et al., 2017). Through simulation, Keskinen et al. (2006) have demonstrated that the evolution of EPBs are considerably different during Q- and D-days. The structuring of EPBs in the postsunset hours during magnetically active periods was found to be significantly different resulting in severe amplitude scintillations on VHF signal (Kakad et al., 2016). This was attributed to the disturbed time modulation of ambient eastward electric field that resulted in very large upward vertical drifts, which influenced the growth and evolution of RT plasma instability. Also, when the perturbation electric field associated with RT instability is strong enough then it can affect the structuring and dynamics of EPBs. However, so far the duration of such active phases of EPBs are not explored.

In the present study, we have used long-term amplitude scintillation observations to investigate the seasonal and solar flux dependence of the occurrence of F-EPBs during both Q- and D-days. We estimate the duration of F-EPBs, which is linked to the active perturbation electric field of RT plasma instability. The possible sources responsible for the midnight fresh generation of EPBs on Q-days are discussed using long-term ionosonde observations and climatological models for electric field. A theoretical model is used to understand the distribution of S_4 index, a measure of strength of scintillation, on ground during Q- and D-days. The data used and analysis technique are discussed in section 2. Identification of F-ESF is described in section 3. Results are explained in section 4. The present work is discussed in section 5 and summarized in section 6.

2. Observations and Analysis Technique

We used amplitude scintillation data for a 251-MHz signal transmitted from a geostationary satellite and recorded by two spaced receivers aligned in the magnetic east-west direction at the dip equatorial station Tirunelveli (8.7°N, 77.8°E, dip latitude 1.5°N) during 1992–2006 and 2013–2015. Geostationary satellite FLEETSAT (73°E) during 1992–2000, UFO2 (71.2°E) during 2000–2006, and UFO10 (72.4°E) during 2013–2015 were transmitting this radio signal. The sampling intervals of scintillation data were 0.1 s (0.05 s) before (after) 2013. Spaced receivers are separated by a distance of 540 m. Although we have used scintillation observations during 1992–2006 and 2013–2015, the experiment was not running in a continuous mode throughout this period. Figure 1 shows the variation of 10.7 cm adjusted solar flux Φ_s (red line) superimposed with the days with scintillations (black circles) and the time intervals of nonfunctioning of the experiment (blue line). It may be noted that we have fairly good observations during solar cycle 23 that covers both low (Φ_s <120) and high (Φ_s >180) solar flux periods. Overall, the amplitude scintillations were seen on 1,403 days. The solar flux data are taken from NGDC NOAA. In addition, we used ionosonde data recorded at nearby dip equatorial station Trivandrum (77°E, 8.5°N, dip 0.5°N) during the period of 1990–2003 that contributed overall 127 months of observations. We have scaled the ionosonde observations to get the base height of F-layer ($h'F$). The ionosonde data are available at the sampling interval of 15 or 5 min. The VHF scintillation experiment is operated by IIG, India, and the ionosonde is operated by the SPL, India. To get estimates of the ambient electric fields at Tirunelveli, we used the real-time model of the ionospheric electric fields proposed by Manoj and Maus (2012) and it is available at http://geomag.org/models/PPEFM/RealtimeEF.html. We also

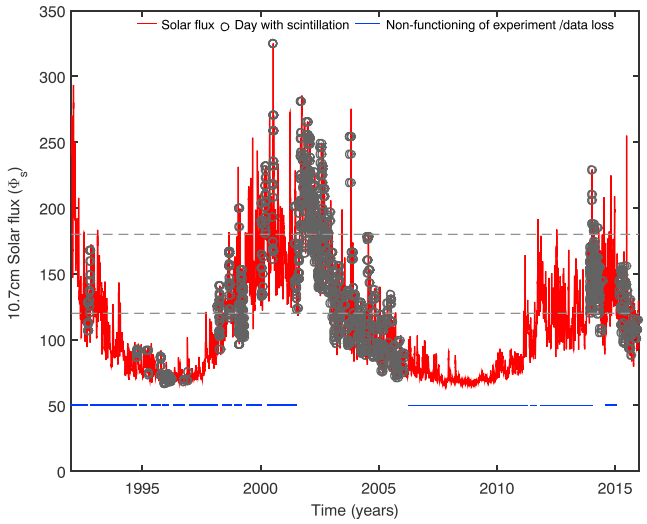

Figure 1. Solar flux variation for the period of 1992–2016 is shown with the days, which encountered amplitude scintillations (black circles) at the dip equatorial station Tirunelveli. The upper and lower black dotted lines indicate the solar flux 120 and 180, respectively. These are the limiting values that are chosen to separate the scintillation observations into different bins based on solar flux.

used HWM2014, NRLMSIS00, and IRI2016 models to retrieve information about the ambient neutral winds, ion-neutral collision frequency, and ionospheric parameters.

We identified the Q- and D-days using midlatitude *Kp* index provided by WDC, Kyoto. Generally, if 3-hourly *Kp* index exceeds 3+ or daily $\sum Kp > 24$ then that interval or day is treated as magnetically disturbed. Occasionally, it can happen that the magnetic disturbance starts later during the day and for such days the resultant $\sum Kp$ might be less than 24. But, the magnetic activity is in place for such days. In addition, earlier studies have witnessed a delayed effect of magnetic activity in low-latitude ionosphere, which is linked with the modulation of electric field and composition changes driven by the DD. So we have adopted the following criteria to separate Q- and D-days; if $\sum Kp$ for a given day or its preceding day is greater than 24 or average *Kp* during 00–09 or 12–24 hr UT greater than 3+ then that day is treated as magnetically disturbed.

Spaced receivers scintillation technique is in use from many years to decipher the dynamics of EPBs (Bhattacharyya et al., 1989; Ledvina et al., 2004; Valladares et al., 1996). We used the full cross-correlation technique introduced by Briggs (1984) to analyze these amplitude scintillations. The space-time correlation function is assumed to have following form,

$$C_l(x,t) = f((x - V_0 t)^2 + V_c^2 t^2). \quad (1)$$

Here f is a monotonically decreasing function of its argument $S = ((x - V_0 t)^2 + V_c^2 t^2)$ with $f(0)=1$. V_0 is the average drift speed of scintillation pattern along the baseline of the receivers in the receivers plane. V_c is referred to as the random velocity, a measure of random changes in the irregularity characteristics. The technique gives S_4, $C_l(x_0, t_m)$, V_0, and V_c, which are computed for every 3 min. S_4 index is defined as the standard deviation of the normalized intensity variations of the received signal and it is a measure of strength of scintillations. $C_l(x_0, t_m)$ is the maximum cross-correlation between intensity variations recorded by the two receivers, which occurred at time lag t_m. We have computed V_0 and V_C only when $C_l(x_0, t_m) \geq 0.5$, as the assumed functional form of f in equation (1) is valid only if signals from two receivers are well correlated. This technique is used to retrieve meaningful information only if the scintillations are well above the noise level, that is, $S_4 \geq 0.15$. This technique and its application to spaced receiver observations are elaborated in Bhattacharyya et al. (1989).

3. Identification of Freshly Generated ESF Irregularities

When we look into the occurrence of EPBs and attribute their generation to local ambient ionospheric conditions one has to be cautious because the observed EPBs might be locally generated or drifted in from some other location. Both drifted and freshly generated ESF can produce amplitude and phase scintillations on radio signal traversing through them. It is an important aspect, which was addressed by Bhattacharyya et al. (2002, 2001). The maximum cross-correlation between intensity variations recorded by two spaced receivers is used to identify the presence of locally generated or F-ESF. Later, this method was adopted in many other studies (Bhattacharyya et al., 2003; Engavale et al., 2005; Kakad et al., 2007; Kakad, Nayak, et al., 2012). In case of radar observations, the maximum spectral width can be used to identify F-EPBs (Tiwari et al., 2006). Using radar observations, an attempt was made to identify the drifted and evolutionary type EPBs by tracking their evolution in the field of view of radar (Ajith et al., 2016).

In the present study, we have identified amplitude scintillation intervals that are associated with F-ESF irregularities for both Q- and D-days. This is done in order to ensure that the ESF irregularity statistics presented here represent the active EPBs. In such study, the identification of F-ESF irregularities is an important task. We have used the parameter $C_l(x_0, t_m)$ to identify the periods of F-ESF on both Q- and D-days. In Figure 2, we have given four examples to illustrate the periods of F-ESF. Figure 2 shows the local time variation of maximum cross-correlation $C_l(x_0, t_m)$ for 2 September 2001, 27 September 2001, 14 November 2015, and 11 August 2015, along with their corresponding monthly quiet time pattern in the background. Here blue dots represent the local time variation of $C_l(x_0, t_m)$ for all quiet days of corresponding month when scintillations

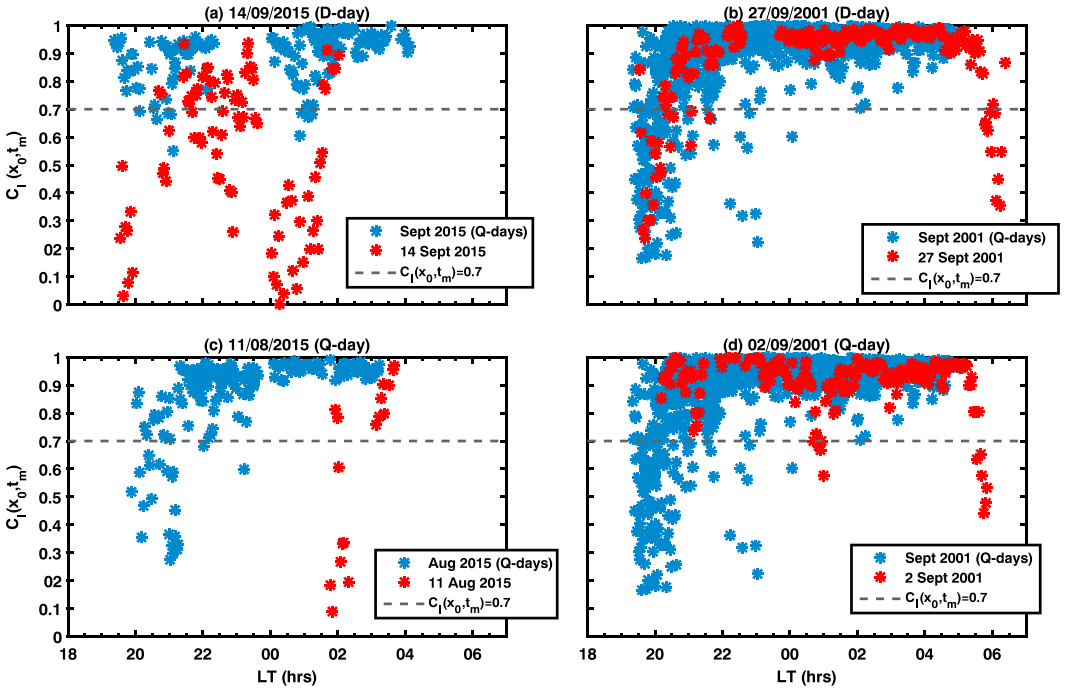

Figure 2. Shows local time variation of maximum cross-correlation between intensity variations recorded by two spaced receivers, that is, $C_I(x_0, t_m)$ for two D-days (upper panel) and two Q-days (lower panels) shown by red asterisks, superimposed on their monthly quiet time variation (blue asterisk). The horizontal dotted line drawn in each panel represents the $C_I(x_0, tm)$ =0.7. The periods with $C_I(x_0, tm)$ ≤0.7 are used to identify the fresh generation of equatorial spread F irregularities. D-day = disturbed day; Q-day = quiet day.

are present. Local time variation of $C_I(x_0, t_m)$ for the 4 days, which are chosen as examples to demonstrate the occurrence of F-ESF even after 22 LT on some D- and Q-days, are shown by red dots. In Figures 2a and 2c, we have a small population of blue dots as year 2015 is low solar activity period and we have few days with scintillations in August and September 2015. It is evident that during the early phase of evolution of EPBs in the postsunset hours, $C_I(x_0, t_m)$ values tend to be lower due to perturbation electric field associated with RT plasma instability. This suggests that random changes take place in the drift velocity of ESF irregularities due to this perturbation electric field during this phase. But, in the later phase (>22 LT) when this perturbation electric field decays considerably, the signals from two receivers have good correlation. Occasionally, lower values of $C_I(x_0, t_m)$ are encountered even after 22 LT, which indicates the fresh generation of ESF during other times as well. This feature is used as a proxy to identify the periods of F-ESF. For each day, scintillation periods with $C_I(x_0, t_m) \leq 0.7$ are considered as the intervals of F-ESF. By, adopting this method, we compiled the database for Q- and D-days, which is analyzed further to retrieve the seasonal and solar flux dependence of these F-ESF.

4. Results

The present study is focused on the occurrence of F-ESF, durations of their active phases, and their role in controlling the strength of scintillations during Q- and D-days. Overall, amplitude scintillations were observed on 397 D-days and 1,006 Q-day. The results obtained from the data are presented in following subsections.

4.1. Local Time Distribution of F-ESF and Strength of Scintillations

The local time variations of percentage occurrence of F-ESF on (a) Q-days and (b) D-days are shown in Figure 3. On Q-days the F-ESF irregularities are dominantly (≈85%) observed in the postsunset hours (18–22 LT), which is the most favorable time of occurrence of EPBs. Whereas on D-days, the F-ESF is prevalent (≈55%) even after 22 LT. The postsunset occurrence of F-ESF on D-days may have some contribution from usual postsunset EPBs, if PRE is unaffected by the magnetic disturbance. If we compare Q- and D-days, we find that the postmidnight occurrence of F-ESF is more likely on D-days as compared to Q-days. This tendency is in general agreement with the earlier studies (Abdu et al., 2003; Kakad et al., 2007; Li et al., 2010) and attributed to the westward to

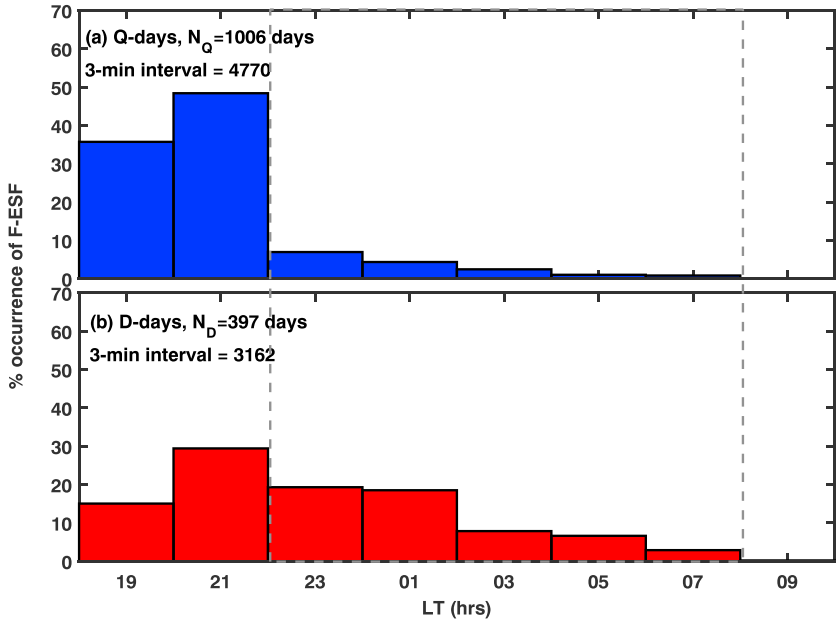

Figure 3. Local time variations of percentage occurrence of F-ESF irregularities for (a) Q-days and (b) D-days. For each category the sum of the percentages shown by each bar adds to 100%, that is, n = 4n770 (n = 3,160) intervals of 3 min for Q-days (D-days). F-ESF = fresh equatorial spread F; Q-days = quiet days; D-days = disturbed days.

eastward reversal of ambient electric field around midnight due to DD electric fields (Fejer & Scherliess, 1997; C.-M. Huang et al., 2005; Richmond et al., 2003). The eastward electric field raises F-layer to higher altitude, where collision frequency of ions is smaller, which can contribute to the growth of RT instability positively, resulting in the generation of F-ESF. As discussed earlier, we are looking at the F-ESF, that is, scintillations associated with $C_l(x_0, t_m) \leq 0.7$. The total number of 3-min intervals contributing to F-ESF are 4,770 and 3,162 for Q- and D-days, respectively. This is an interesting feature because number of D-days are much less compared to Q-days. But still the duration of scintillation events associated with F-ESF are nearly comparable for both Q- and D-days. It suggests that the F-ESF duration is longer on D-days. This feature is discussed in detail in section 4.2.

Now in order to examine the distribution of strength of scintillations caused due to these F-ESF, we divided observations into three categories based on S_4 index such that (i) $0.15 \leq S_4 < 0.5$, (ii)$0.5 \leq S_4 < 1$, and (iii) $S_4 \geq 1$, respectively, indicate weak, moderate–strong, and saturated scintillations. The percentage occurrence of F-ESF for these categories are compared for Q- and D-days during (a) early (18–22 LT) and (b) later (>22 LT) phases of the evolution of these irregularities, in Figure 4. It is clearly evident that the occurrence of moderate–strong scintillations is considerably higher for F-ESF triggered on D-days during both early and later phases, which is marked by dotted rectangular box. It means that F-ESF irregularities generated on D-days can cause more degradation to the radio signal passing through them. This feature directly hints toward the difference in the spatial structuring of F-ESF on D-days as compared to Q-days, which may be attributed to difference in ambient ionospheric conditions. In other words, the altitudinal extent of the irregularities over the dip equator, the irregularity power spectrum, and density perturbations are expected to be different for F-ESF generated on Q-days and D-days. A study carried out by Keskinen et al. (2006) support this possibility as considerable difference in the evolution of postsunset EPBs is noticed in their computer simulation on D-days. So we have further explored this discrepancy with the help of a theoretical model, which is explained in section 5.2.

4.2. Duration of Active Phase of ESF

The ESF irregularities keep evolving from the time of their generation till their decay. The characteristics of ESF irregularities change rapidly when the perturbation electric field associated with plasma instability is significant to influence their dynamics. This is manifested in the quiet time mass plot of $C_l(x_0, t_m)$, shown in Figure 2 (blue color). In the postsunset hours, when the ESF irregularities are generated, values of $C_l(x_0, t_m)$ are found to be lower as compared to the later phase. As discussed in section 3, such tendency clearly indicates that

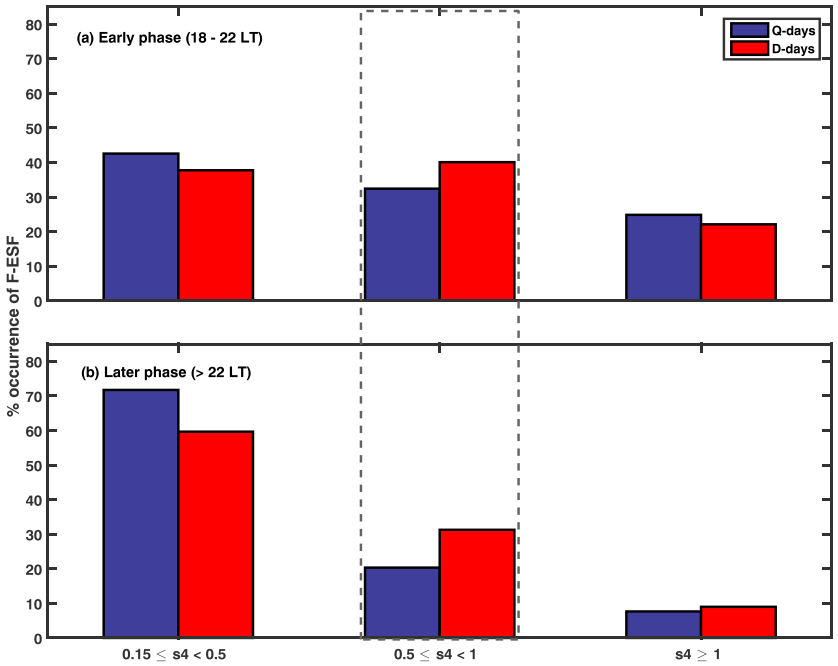

Figure 4. The percentage occurrence of F-ESF associated scintillations having different strengths, namely (i) weak, $0.15 \leq S_4 < 0.5$; (ii) moderate–strong, $0.5 \leq S_4 < 1$; and (iii) saturated, $S_4 \geq 1$, are plotted for (a) early phase, 18–22 LT, and (b) later phase, >22 LT, of evolution of ESF irregularities occurring on both Q-days (blue bars) and D-days (red bars). S_4 index is a measure of strength of amplitude scintillations. For early (18–22 LT) and later (>22 LT) phases separately, the sum of the percentages shown by each bar adds to 100%. It means the blue (Q-days) and the red (D-days) bars will add to 100% in both upper and lower panels. F-ESF = fresh equatorial spread F; Q-days = quiet days; D-days = disturbed days.

the characteristics of the ESF irregularities are changing faster during their initial phase of development after initiation of the RT plasma instability. However, in the later phase (>22 LT) the ESF irregularity characteristics vary slowly due to weakening of perturbation electric field that results in higher values of $C_l(x_0, t_m)$. Thus, the duration of F-ESF can be considered as the measure of active phase of the ESF irregularities, where the perturbation electric field is alive.

We estimated the duration of F-ESF using $t_d = N_p \times 3$, where N_p indicates the number of 3-min interval with $C_l(x_0, t_m) \leq 0.7$ for a given day. Here t_d is expressed in minutes. The percentage of days having t_d in different ranges are shown in Figure 5 for (a) early phase (18–22 LT) and (b) later phase (>22 LT) on Q-days and D-days. The number of days in each category are mentioned on respective bars. In general, the duration of F-ESF is found to be significantly longer on D-days as compared to Q-days in both early and later phases. On Q-days 90–92% of F-ESF events have durations of 9–60 min, during both early and later phases. Only approximately 8–10% of the F-ESF events on Q-days have durations of 60–120 min. Whereas, on D-days approximately 16–29% of F-ESF events are found to be active for durations of 60–120 min. The duration of F-ESF is even longer than 120 min on about 10% of D-days.

As discussed earlier, F-ESF duration can be associated with the active perturbation electric field of the RT plasma instability. Thus, it implies that the perturbation electric field linked with the RT plasma instability sustains for longer durations on D-days as compared to Q-days. The strength, time variation, and survival of the perturbation electric field is controlled by both growth and decay mechanisms involved in the evolving plasma instability and temporal variation of the ambient ionosphere. In the growth phase the perturbation electric field associated with the instability is expected to get modified. The growth time of RT plasma instability is nearly 10–60 min (Kelley et al., 1979; Yokoyama, 2017), which is of the same order as that of F-ESF durations reported here for the early phase. It is known that the ambient electric field is a key parameter that plays an important role in the initial linear growth of RT plasma instability (Kelley et al., 1981). Thus, the presence of substantial perturbation electric field for longer durations on D-days is attributed to the magnetic activity linked ambient ionospheric electric fields.

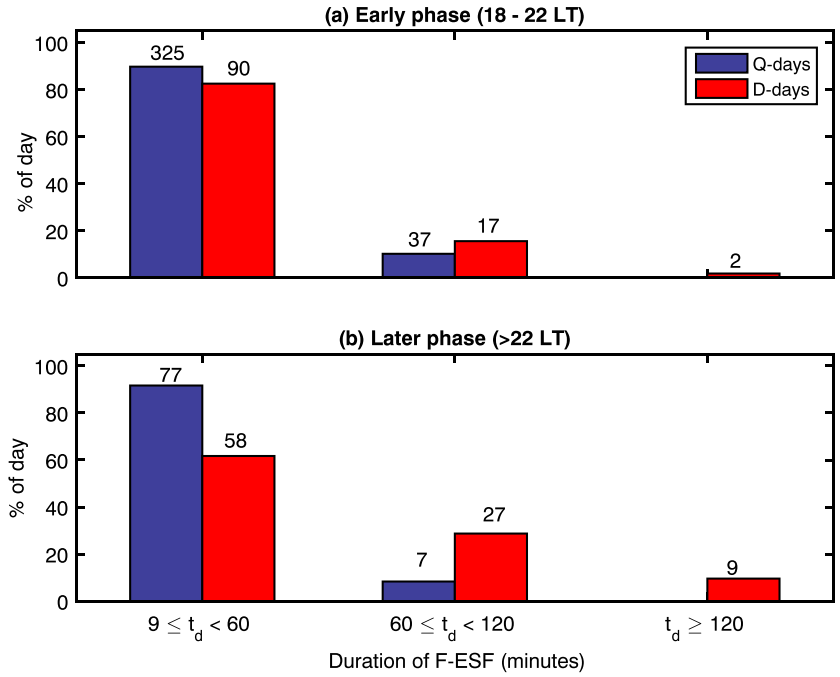

Figure 5. Percentage of Q- and D-days having duration of F-ESF in the range of (i) $9 \leq t_d < 60$, (ii) $60 \leq t_d < 120$, and (iii)$t_d \geq 120$ are shown here for both (a) early phase, 18–22 LT, and (b) later phase, >22 LT, of evolution of ESF irregularities. The duration of F-ESF represent the active phase of equatorial plasma bubbles, where the perturbation electric field associated with Rayleigh Taylor plasma instability is alive. On D-days, the duration of F-ESF is found to be longer as compared to Q-days. For early (18–22 LT) and later (>22 LT) phase separately, the sum of the percentages of number of days with different t_d shown by each bar adds to 100%. It means the blue (Q-days) and the red (D-days) bars will each add up to 100% in both upper and lower panels. F-ESF = fresh equatorial spread F; Q-days = quiet days; D-days = disturbed days.

4.3. Seasonal and Solar Flux Variation of F-ESF

In this section we have examined the seasonal and solar flux dependence of the local time occurrence of F-ESF. The postmidnight occurrence of F-ESF on D-days has been reported earlier (Bhattacharyya et al., 2002; Kakad et al., 2007) but their seasonal and solar flux dependence is not studied. First, we have divided the F-ESF observations into three bins of solar flux, namely low ($\phi_s \leq 120$), moderate ($120 < \phi_s \leq 180$), and high $\phi_s > 180$. Later, for each bin of solar flux, we separated F-ESF observations for different seasons like March–April (MA), September–October (SO), November–February (NDJF), and May–August (MJJA). This analysis is carried out separately for both Q- and D-days. Figures 6 and 7 show the local time occurrence of F-ESF for different seasons for low, moderate, and high solar flux periods for Q- and D-days, respectively. We have overall 475 days, 609 days, and 319 days in low, moderate, and high solar flux categories, respectively. On Q-days, one can see that the occurrence of F-ESF is most prevalent in the postsunset period (18–22 LT) in all seasons except for the solstice of low solar activity periods. We find that in both solstices during the postmidnight hours (00–04 LT) occurrence of F-ESF is considerable during low solar activity, which is marked by black rectangle. In addition, on some occasions the early-morning (>04 LT) F-ESF is encountered during high solar activity period, which is marked by red rectangle. A clear local time dependence of occurrence of F-ESF is revealed for the Q-days. Particularly, for Q-days the F-ESF dominantly occur in the postsunset time, but in solstice months favorable time of F-ESF is also found to be in the postmidnight hours during low solar activity. The midnight occurrence of ESF during local summer months has been reported in earlier studies (Sastri, 1999; J. M. Smith et al., 2016). Niranjan et al. (2003) have reported ESF irregularities during both summer (May–August) and winter (November–February) solstice using ionosonde observations from a low-latitude Indian station. In their study the occurrence of midnight ESF was found to be smaller during winter (≈37%) as compared to summer (≈63%). In all these studies no attempt was made to distinguish between freshly generated and drifted ESF irregularities. Recently, Ajith et al. (2016) studied the evolving and drifted EPBs observed by equatorial atmosphere radar (47 MHz) in Indonesia and found that the evolving EPBs, which may be considered as freshly generated in the field of view of radar, are dominantly seen around midnight (≈01 LT) in June solstice of low

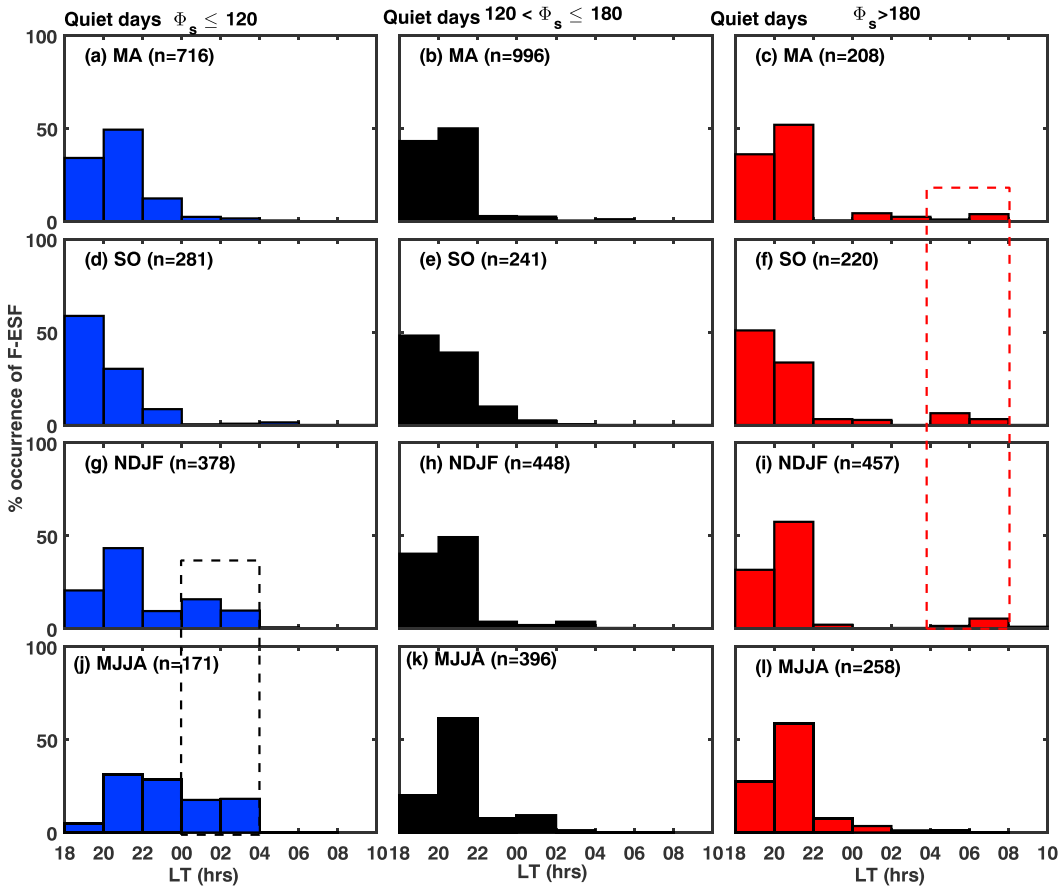

Figure 6. Shows local time variation of percentage occurrence of F-ESF for different levels of solar flux, namely (i) low $\Phi_s \leq 120$, (ii) moderate $120 < \Phi_s \leq 180$, and (iii) high $\Phi_s > 180$, and for different seasons MA, SO, MJJA, and NDJF for quiet days. Black and red rectangular dotted boxes, respectively, represent the midnight (00–04 LT) and early-morning (>04 LT) generation of F-ESF during low and high solar activity periods. The midnight F-ESF is observed more frequently for solstice months of low solar activity. In each subplot, the addition of percentages shown by bars gives 100% and it corresponds to total number of 3-min interval (i.e., *n*) mentioned in each subplot. F-ESF = fresh equatorial spread F; MA = March–April; SO = September–October; NDJF = November–February; MJJA = May–August.

solar activity period 2010–2012, whereas such midnight EPBs are less frequent during December solstice. In present study we find that the postmidnight (00–04 LT) occurrence F-ESF is comparable during both June (≈36%) and December (≈26%) solstice of low solar activity.

For D-days the occurrence of F-ESF does not show clear season or solar flux dependence. Figure 7 indicates that in general the magnetic activity linked generation of F-ESF is dominantly observed in the postmidnight and early-morning hours. The magnetic activity linked DD and PP electric fields are the main sources for the modulation of ionospheric electric fields on D-days. The strength and spatial distribution of these DD and PP electric fields are governed by the start time, strength, and nature of magnetic activity and it varies with each magnetic activity. Theoretical and simulation studies have shown that the DD electric field is eastward around local midnight sector (C.-M. Huang et al., 2005; Richmond et al., 2003). C. M. Huang (2013) has shown that the amplitude of DD electric field varies with solar flux and season, however its tendency to reverse from west to east is seen around the local midnight hours. Thus, we can expect the presence of eastward electric field on D-days around local midnight, which can assist the generation of F-ESF. However, the scenario can be completely different if the DD electric field is modified by the presence of PP electric fields (N. Maruyama et al., 2005). It is shown that the effects in low-latitude ionosphere in a given longitudinal sector can be different for nearly similar storms starting at different times (Kakad et al., 2017).

In order to understand the postsunset occurrence of F-ESF during both Q- and D-days, we estimated the overall percentage occurrence of F-ESF during 18–22 LT for different seasons during low, moderate, and high solar

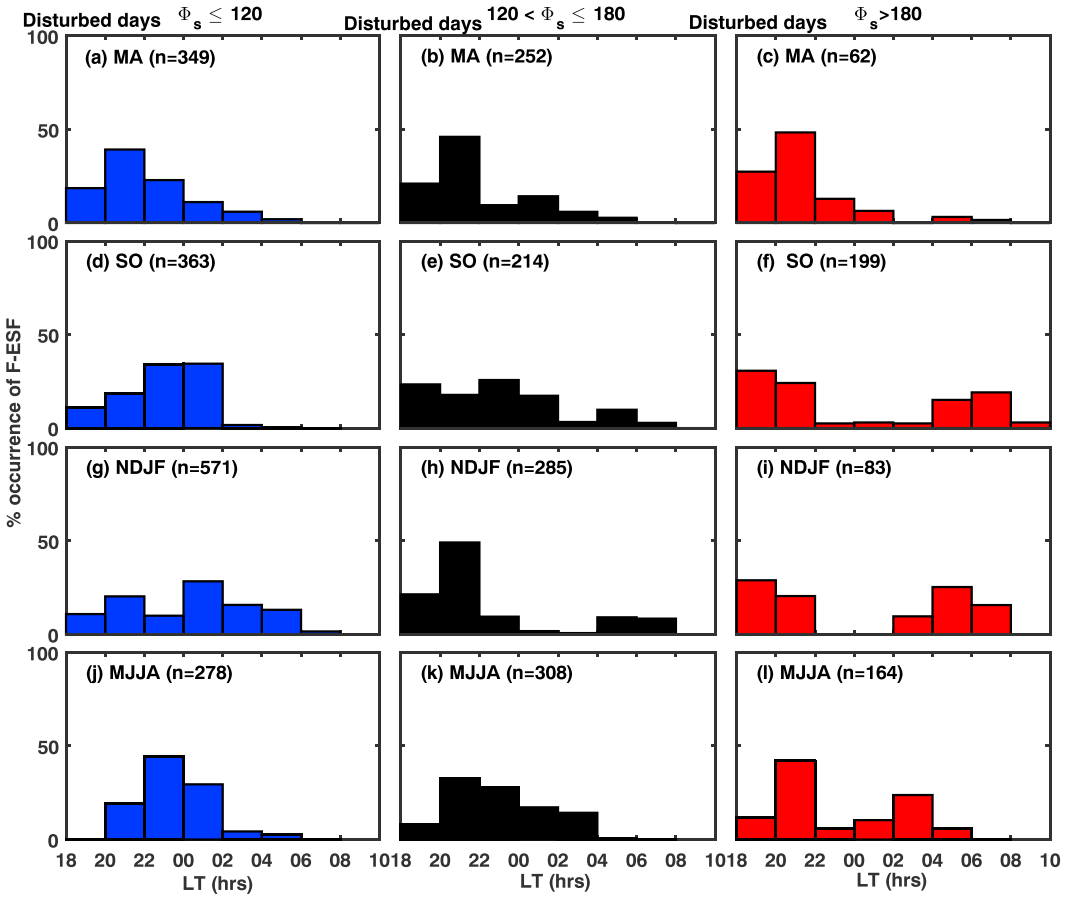

Figure 7. Shows local time variation of percentage occurrence of F-ESF for different levels of solar flux, namely (i) low $\Phi_s \leq 120$, (ii) moderate $120 < \Phi_s \leq 180$, and (iii) high $\Phi_s > 180$, and for different seasons MA, SO, MJJA, and NDJF for disturbed days. In each subplot, the addition of percentages shown by bars gives 100% and it corresponds to total number of 3-min interval (i.e., *n*) mentioned in each subplot. F-ESF = fresh equatorial spread F; MA = March–April; SO = September–October; NDJF = November–February; MJJA = May–August.

activity periods, which is depicted in Figure 8. Top and bottom panels, respectively, represents the F-ESF occurring on Q- and D-days. Blue, black, and red colors represent low, moderate, and high solar activity periods, respectively. For a given season and solar flux condition (i.e., low/moderate/high), we estimated the number of 3-minute scintillation intervals of F-ESF (i.e., $C_l(x_0, t_m) \leq 0.7$) during 18–22 LT to obtain these percentages. Each bar can attain a maximum of 100% if all scintillation events under that category have $C_l(x_0, t_m) \leq 0.7$, that is, if the observed scintillation were caused entirely by locally generated irregularities. For each level of solar flux, it is found that the postsunset occurrence of F-ESF is higher on Q-days as compared to D-days irrespective of the season. For Q-days, F-ESF is dominantly seen in the postsunset hours (18–22 LT), with occurrence exceeding 80% for all seasons and solar flux levels except for solstice months of low solar activity. Whereas for D-days, the F-ESF occurrence in the postsunset hours is smaller (<80%). It is because EPBs are generated even after 22 LT due to ionospheric electric fields associated with magnetic activity. From Figure 8a, we understand that on Q-days of low solar activity significant reduction in the usual generation of postsunset F-ESF is noticed during solstice months as compared to equinoctial months, which is marked by black arrows. But this reduction is much larger for summer as compared to winter. For summer solstice only 31% occurrence of F-ESF is seen in the postsunset hours, which indicates that nearly 69% of F-ESF occurred in the later hours during the night (>22 LT). For winter solstice the postsunset occurrence of F-ESF is found to be 64%, so nearly 36% occurrence of F-ESF is observed after 22 LT. In section 5 we discuss the possible sources for the midnight F-ESF during both solstices. If we compare equinoctial months, the total occurrence of F-ESF in postsunset hours during March–April (Vernal equinox) and September–October (Autumn equinox) is found to be 91% and 86%, respectively, for moderate to high solar activity periods. For low solar activity periods, this tendency is reversed, the total occurrence of F-ESF in postsunset hours during March–April (83%) is found to be lower as

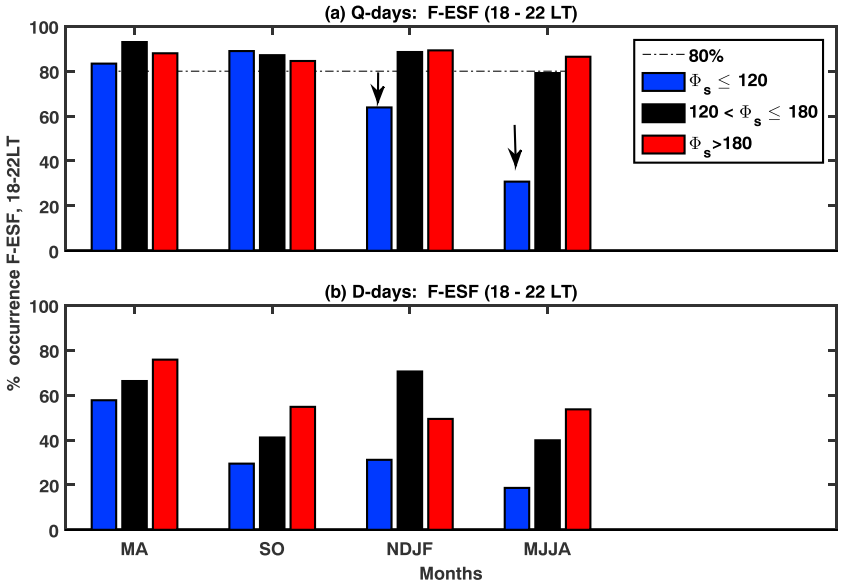

Figure 8. Total percentage occurrence of F-ESF during early phase (18–22 LT) for different seasons on (a) Q-days and (b) D-days during low (blue), moderate (black), and high (red) solar activity periods. Horizontal dashed-dotted lines indicate the percentage occurrence of 80%. Each bar corresponds to percentage occurrence of F-ESF for given season, solar flux condition (i.e., low/moderate/high) during early phase (i.e., 18–22 LT). Each bar can attain maximum of 100% if intervals with scintillations under that category have $C_l(x_0, t_m) \leq 0.7$. F-ESF = fresh equatorial spread F; Q-days = quiet days; D-days = disturbed days; MA = March–April; SO = September–October; NDJF = November–February; MJJA = May–August.

compared to September–October (89%). This difference in the percentage occurrence of F-ESF for equinoctial months is not significant enough to attribute it to equinoctial asymmetry reported by Sripathi et al. (2011).

5. Discussion

In this section we discuss two observational features, (i) postmidnight occurrence of F-ESF during solstices of low solar activity and (ii) larger occurrence of moderate–strong scintillations due to F-ESF occurring on D-days as compared to Q-days.

5.1. Understanding Solstice Midnight F-ESF

It is known that height of F-region plays an important role in setting up a favorable ambient ionospheric condition for the growth of RT plasma instability. The altitude of the F-region is controlled by the ambient electric field through $\vec{E} \times \vec{B}$ vertical drifts. The results shown in previous subsection indicates two features, (i) F-ESF generation around midnight and (ii) considerable decrease in usual postsunset occurrence of F-ESF during summer solstice of low solar activity. In order to understand these tendencies, we examined the variation of $h'F$ from near by dip equatorial station Trivandrum using long-term ionosonde observations. The scaled values of $h'F$ are separated into three categories based on the levels of solar flux and average virtual base height of F-region is estimated for different seasons. The local time variation of average base height of F-region during low solar activity ($\Phi_s \leq 120$) is shown in Figure 9a for different seasons. The standard deviation in the averaged values of base height of F-region is in the range of 5–50 km. It is clearly evident that postsunset PRE is suppressed during summer solstice with enhancement in F-region altitude around midnight. Such enhancement in F-region altitude around midnight can aid the development of F-ESF, in the presence of appropriate triggering source needed for the RT plasma instability. However, we do not see such midnight F-region height rise for winter. We also looked into local time variation of ambient zonal ionospheric electric fields at Tirunelveli, which are obtained from the real-time ionospheric model given by Manoj and Maus (2012). Figure 9b shows the local time variation of zonal electric field (+*ve* eastward) for different seasons during low solar activity ($\Phi_s \leq 120$). In Figure 9b it is noticed that although the zonal electric field is westward around midnight for the both solstices and equinoctial months, the westward electric field is weaker for solstices compared to equinoctial months. Based on the ionosonde observations in Figure 9a, where a clear midnight F-region height rise is observed for the June solstice, one expects an eastward electric field around midnight, while the model

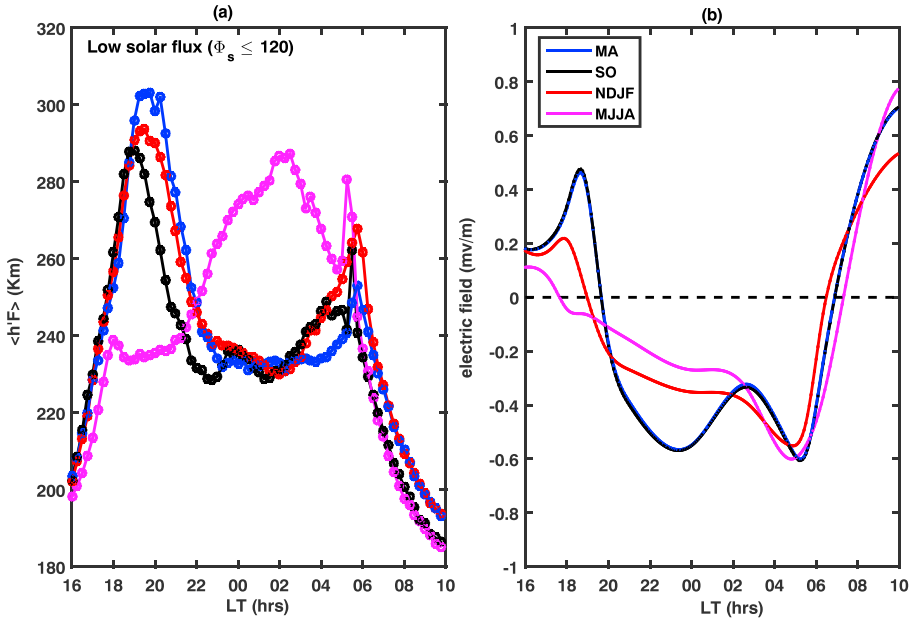

Figure 9. Shows quiet time seasonal local time variation of (a) averaged values of $h'F$ observed at Trivandrum and (ii) ambient zonal electric field derived from real-time ionospheric model (http://geomag.org/models/PPEFM/RealtimeEF.html) for low solar activity ($\Phi_s \leq 120$). The standard deviation in $h'F$ is in the range of 5–50 km. MA = March–April; SO = September–October; NDJF = November–February; MJJA = May–August.

results fail to match these observations. But at least they show that around midnight of summer solstice the westward electric field is the weakest compared to other seasons. Hence, even a weak source of eastward electric field either from above or below the ionosphere is sufficient to reverse the polarity of zonal electric field from westward to eastward around midnight of summer solstice in the Indian region.

It has been shown that trans-equatorial neutral wind plays an important role in the occurrence of ESF as it can influence the postsunset PRE. A stronger poleward or weaker equatorward neutral wind suppress the amplitude of PRE (Abdu et al., 2006). A stronger equatorward meridional wind pushes the ionization from low-latitudes to equatorial-latitudes and raises the F-layer to higher altitudes over equatorial stations. It is shown that meridional neutral winds converge toward equator around local midnight during summer months of Northern Hemisphere (i.e., equatorward wind), which can assist the generation of F-ESF (T. Maruyama et al., 2008; Sripathi, 2017). Studies have suggested that the local midnight temperature maximum and sudden stratospheric warming events assist the formation of F-ESF around local midnight in summer (Niranjan et al., 2003; J. M. Smith et al., 2016). Both midnight temperature maximum and sudden stratospheric warming events modulate the background neutral wind patterns. The altitudinal variation of meridional wind derived from horizontal wind model for 1 day representing summer and winter solstice is shown in upper panels of Figure 10 for low solar activity period ($\Phi_s = 86$). These winds are estimated at 15°N geographic latitude and 77.8°E geographic longitude. Positive values represent poleward winds. The black solid (dotted) line represents the average meridional wind for the altitudes 200–250 km (250–300 km). It is noticed that the meridional winds are equatorward (poleward) for summer (winter) solstice around midnight. It implies that favorable neutral winds are not present at off-equatorial locations around local midnight during winter to assist the generation of F-ESF. Further, to understand the difference in other ambient F-region parameters affecting the linear growth of RT plasma instability, we examined the (i) ion-collision frequency (ν_{in}), (ii) inverse scale length $L^{-1} = [\frac{1}{n_0}\frac{\delta n}{\delta z}]$, and (iii) R factor, which is defined as $[\nu_{in}L]^{-1}$. We used NRLMSIS00 and IRI2016 models to get these parameters for Tirunelveli and they are shown in second, third, and fourth panels of Figure 10. The altitudinal and time resolutions for Figure 10 are 1 km and 6 min, respectively. The black dotted and solid lines in each subplot of Figure 10, respectively, represent the average of corresponding parameter for the altitudes 250–300 and 200–250 km. The linear growth rate of RT plasma instability is proportional to R factor. It

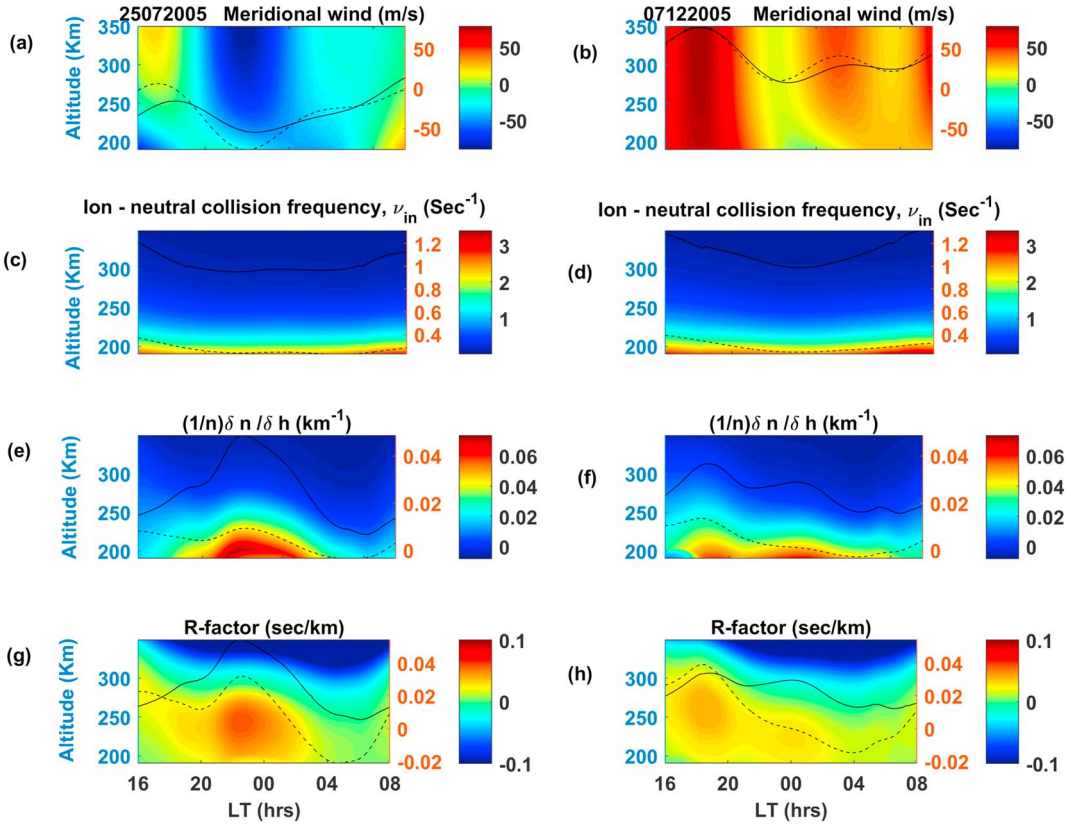

Figure 10. Shows local time variation of meridional winds (+ve northward), ion-neutral collision frequencies ν_{in}, inverse scale length $L^{-1} = \frac{1}{n}\frac{\delta n}{\delta z}$, and parameter $R = [\nu_{in}L]^{-1}$ for altitudes 190–350 km. Left-side (right-side) panels represent typical conditions during summer (winter) solstice. These parameters are derived from HWM2014, IRI2016, and NRLMSIS00 models for low solar activity period Φ_s=86. Meridional winds are obtained for a location in Northern Hemisphere away from the observation station (geographic latitude 15°N, geographic longitude 77.8°E), whereas all other parameters are obtained for Tirunelveli (geographic latitude 8.7°N geographic longitude 77.8°E). Solid and dotted curves in each subplot, respectively, represent the average of that parameter for 200–250 and 250–300 km.

may be noted that *R* factor shows enhancement close to local midnight in summer and it can positively assist the growth of RT plasma instability to generate ESF irregularities. On the other hand, *R* factor is only weakly positive around local midnight during winter as compared to summer. So local ambient F-region parameters around local midnight can positively support the generation of F-ESF in summer as compared to winter.

5.2. Difference in S_4 Distribution: Theoretical Explanation

The strength of scintillation is measured in terms of S_4 index and it is controlled by ambient ionospheric parameters. A theoretical model suggests that the power spectral characteristics, density perturbations associated with ESF irregularities, height, and thickness of irregular medium controls the phase fluctuations imposed on radio signal and hence affects the distribution of S_4 on ground (Engavale & Bhattacharyya, 2005). In order to understand the difference in the S_4 distribution, we used this theoretical model. It is a stationary model that divides a thick irregularity layer into number of thin phase screens separated by diffraction layers, and then the propagation of radio wave through this irregular medium is examined to get information about the S_4 in the receiver's plane. The implementation of such multiple phase screens in the model is accomplished by using Split step algorithm (Bhattacharyya & Yeh, 1988). This model has various input parameters like height (*Z*), thickness (*L*), density perturbation (ΔN), power spectral slope (*m*), outer scale R_0, and inner scale (*r*). We considered thickness of irregularity layer as 50 km and height in the range of 300–600 km. It is known from in situ observations that irregularities have a power law spectrum. Studies have reported that irregularity spectrum does evolve with time and affect the strength of scintillation (Costa & Basu, 2002). Kakad, Nayak, et al. (2012) have reported that F-ESF irregularities producing weak scintillation ($S_4 \leq 0.5$) are mainly associated with power spectral indices between 3 and 4. Thus, we took power spectral index to be m =3 and m =4 for the intermediate scale irregularity spectrum. As we are examining intermediate scale F-ESF irregularities (100 m

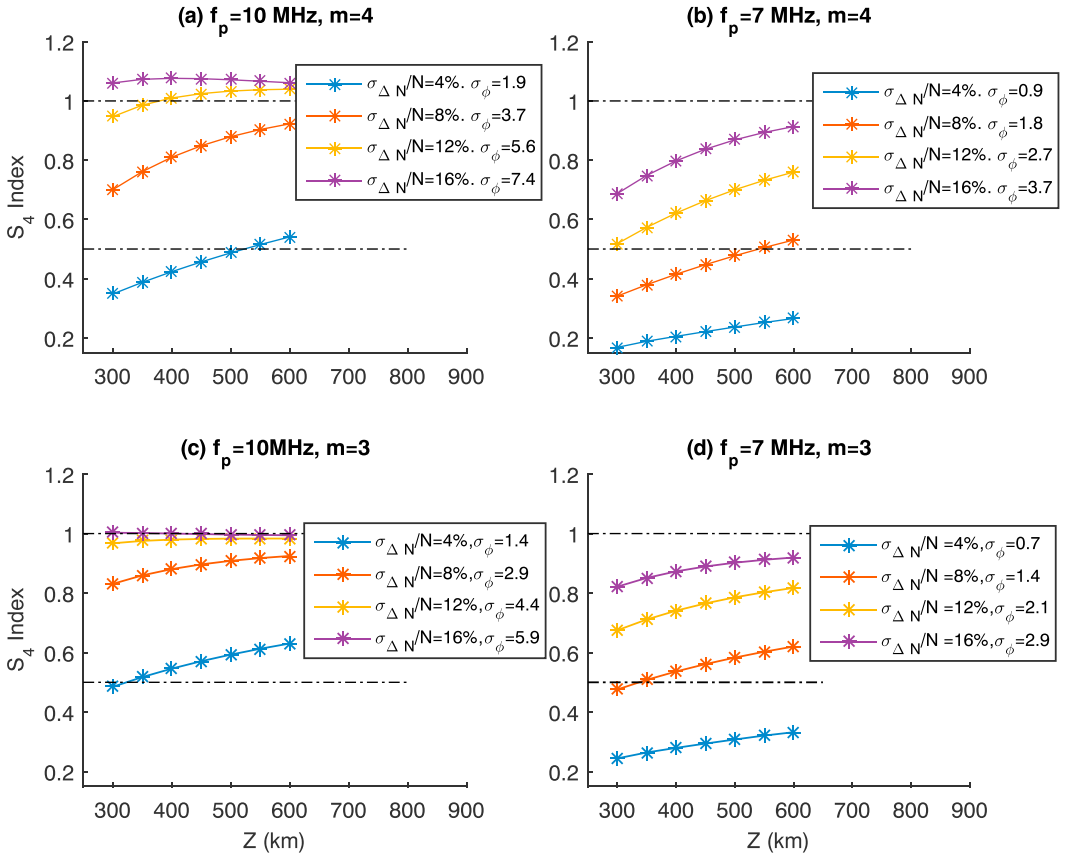

Figure 11. Shows variation of S_4 index as a function of altitude for equatorial spread F irregularities having power spectrum, that is, m =4 (upper panels) and m =3 (lower panels) and different percentage density perturbations ($\sigma_{\Delta N}/N$). The ambient plasma density is taken as 7 (b and d) and 10 MHz (a and c). The upper and lower horizontal dashed-dotted lines represent the S_4 = 1 and S_4 = 0.5, respectively. The corresponding standard deviation of phase fluctuations (in radian) imposed on the radio signal is mentioned in each subplot.

to few km), the outer scale for the power spectrum is taken as 5 km and inner scale considered as 50 m. The ambient plasma frequency is taken as 10 and 7 MHz to represent high and low solar activity. We varied standard deviation of normalized density fluctuation ($\sigma_{\Delta N}/N$) from 4% to 16% and estimated the S_4 in receivers plane.

The plot of S_4 as a function of height of irregularity layer for power spectral indices m =4 and m =3 are shown in Figure 11. The right-side panels are associated with lower ambient plasma density (plasma frequency f_p = 7 MHz), whereas left-side panels correspond to higher ambient plasma density (f_p = 10 MHz). It is noted that larger density fluctuations impose larger phase perturbations on the incident radio signal and produce higher S_4. When ambient plasma density is smaller, that is, f_p =7 MHz (Figures 11b and 11d), for same percentages of density perturbation smaller values of S_4 are produced as compared to the background of higher plasma density, that is f_p =10 MHz (Figures 11a and 11c). It is clearly evident that for irregularities with shallower power spectrum, m = 3S_4 index does not exceed one. When density fluctuations are the same the higher height of irregularity layer helps to produce stronger scintillations, but this altitudinal dependence tends to vanish when S_4 reaches values close to one. Now we understand that intermediate scale irregularities with larger density fluctuations placed at higher altitudes in the presence of stronger ambient plasma density are likely to produce more moderate to strong ($0.5 \leq S_4 < 1$) scintillations. It implies that intermediate scale irregularities with larger density perturbations are available at higher altitudes to produce more moderate–strong amplitude scintillations on the VHF signal during D-days. Although sometimes, the F-ESF is generated in the postmidnight periods on Q-days as well but they are not producing more moderate–strong amplitude scintillations. This can be attributed to the lower altitudinal extent of F-ESF on Q-days as compared to F-ESF on D-days.

6. Summary and Conclusion

The seasonal, solar flux, local time, global occurrence of EPBs are reported in many earlier studies. However, in these studies no attempt was made to separate the locally generated and drifted ESF irregularities. In the present study, we have investigated the occurrence and evolution of only F-ESF. We used the parameter $C_l(x_0, t_m)$ to identify the periods of F-ESF on both Q- and D-days. We have studied seasonal and solar flux dependence of the occurrence of F-ESF during both Q- and D-days using long-term spaced receiver scintillation observations from Indian equatorial station Tirunelveli. As we are using VHF (251 MHz) amplitude scintillations, we get information about intermediate scale 100 m to few kilometers ESF irregularities. Apart from the occurrence of F-ESF, the degradation caused by these irregularities to incoming radio signal is also examined by estimating the S_4 index distribution in the receiver's plane. The duration of F-ESF, which represents the active phase of locally generated ESF, is estimated. In other words, the duration of F-ESF gives information about the life time of the perturbation electric field associated with the RT plasma instability, which is responsible for the generation of these irregularities. Above mentioned two points, that is, (i) degradation caused by F-ESF and (ii) duration of active phase of ESF, are the new aspects that we have investigated in the present study. Various observational features of F-ESF, for different seasons, and solar flux, local time, quiet, and disturbed conditions reported here, are examined using long-term ionosonde observations, real-time ionospheric model (electric fields), and theoretical model (S_4 index) for better understanding. Following are the major conclusions drawn from the present study.

1. Distinct differences in the seasonal and solar flux dependence of the usual postsunset (18–22 LT) generation of F-ESF on both Q- and D-days are noticed. On Q-days the occurrence of F-ESF is mainly confined in the postsunset hours (≈85%). But on D-days the occurrence of F-ESF during early, 18–22 LT (≈45%), and later phase, >22 LT (≈55%), are comparable.
2. On Q-days of low solar activity both solstices encountered significant reduction in the usual postsunset occurrence. In summer the reduction is 54% and for winter it is 21% as compared to equinoctial months. It is because the PRE is not strong during summer to raise the F-region to higher altitudes particularly during low solar activity (Kakad, Tiwari, et al., 2012).
3. On Q-days the postmidnight F-ESF is seen mainly during solstices of low solar activity. The midnight F-ESF observed during summer solstice of low solar activity period is attributed to the increase in F-region height, however, such midnight F-region height rise is not seen for winter to support the generation of F-ESF around midnight during this season. For both solstices the ambient zonal electric fields are found to be weakly westward around midnight, so even smaller strength superposed eastward electric field from some other source is sufficient to reverse the polarity of zonal electric fields from westward to eastward. We need further investigation to understand the sources responsible for the generation of midnight F-ESF particularly during winter solstice.
4. We found that F-ESF linked moderate–strong scintillations are dominant on D-days as compared to Q-days in both early (18–22 LT) and later (>22 LT) periods. It has direct link to the structuring and evolution of EPBs. Theoretical model suggests that the intermediate scale irregularities with strong density perturbations situated at higher altitudes can cause more moderate–strong amplitude scintillations on D-days. Whereas on Q-days, the postmidnight F-ESF do not have larger altitudinal extent to produce more moderate–strong amplitude scintillations.
5. On magnetically D-days, the occurrence of F-ESF is likely around midnight and early-morning hours in all seasons and this local time occurrence pattern is less significantly affected by the solar flux. A simulation study by C. M. Huang (2013) suggests that strength of DD electric field changes with solar flux and seasons, however its reversal from west to east occurs close to local midnight hours. Even with slightly weaker eastward DD electric field, F-region can be raised to higher altitudes around midnight as the westward ambient ionospheric electric fields are also weaker around that time.
6. An important feature is that the perturbation electric field linked with the RT plasma instability, which is responsible for the generation of fresh ESF irregularities, sustains for a longer duration on D-days as compared to Q-days. It results in longer durations of the active phase of EPBs on D-days as compared to Q-days.

Acknowledgments
We thank WDC Kyoto for geomagnetic activity indices and NASA NGDC team for solar flux data. We thank V. Yadav for the help on ionosonde data scaling. We are thankful to K. U. Nair, K. Jeeva, and Ananthi for the technical support to VHF spaced receiver experiment. We thank CIRES for real-time ionospheric model data. GSFC NASA team for HWM2014, IRI2016, and NRLMSIS00 models. A. B. acknowledges Indian National Science Academy for an INSA senior scientist position at IIG. VHF scintillation experiment was operated by IIG, New Panvel, India, and the data are available at DOI: https://doi.org/10.5281/zenodo.1402938

References

Abdu, M. A., Batista, I. S., Takahashi, H., MacDougall, J., Sobral, J. H., Medeiros, A. F., et al. (2003). Magnetospheric disturbance induced equatorial plasma bubble development and dynamics: A case study in Brazilian sector. *Journal of Geophysical Research*, *108*(A12), 1449. https://doi.org/10.1029/2002JA009721

Abdu, M., de Paula, E. R., Batista, I. S., Reinisch, B. W., Matsuoka, M. T., Camargo, P. O., et al. (2008). Abnormal evening vertical plasma drift and effects on ESF and EIA over Brazil-South Atlantic sector during the 30 October 2003 superstorm. *Journal of Geophysical Research*, *113*, A07313. https://doi.org/10.1029/2007JA012844

Abdu, M. A., Iyer, K. N., de Medeiros, R. T., Batista, I. S., & Sobral, J. H. A. (2006). Thermospheric meridional wind control of equatorial spread F and evening prereversal electric field. *Geophysical Research Letters*, *33*, L07106. https://doi.org/10.1029/2005GL024835

Ajith, K. K., Tulasi Ram, S., Yamamoto, M., Otsuka, Y., & Niranjan, K. (2016). On the fresh development of equatorial plasma bubbles around the midnight hours of June solstice. *Journal of Geophysical Research: Space Physics*, *121*, 9051–9062. https://doi.org/10.1002/2016JA023024

Basu, S., et al. (1996). Scintillations, plasma drifts, and neutral winds in the equatorial ionosphere after sunset. *Journal of Geophysical Research*, *101*(A12), 26,795–26,809.

Bhattacharyya, A. (2004). Role of E region conductivity in the development of equatorial ionospheric plasma bubbles. *Geophysical Research Letters*, *31*, L06806.

Bhattacharyya, A., Basu, S., Groves, K. M., Valladares, C. E., & Sheehan, R. (2001). Dynamics of equatorial F region irregularities from spaced receiver scintillation observations. *Geophysical Research Letters*, *28*(1), 119–122. https://doi.org/10.1029/2000GL012288

Bhattacharyya, A., Basu, S., Groves, K. M., Valladares, C. E., & Sheehan, R. (2002). Effect of magnetic activity on the dynamics of equatorial F region irregularities. *Journal of Geophysical Research*, *107*(A12), 1489. https://doi.org/10.1029/2002JA009644

Bhattacharyya, A., Franke, S., & Yeh, K. (1989). Characteristic velocity of equatorial F region irregularities determined from spaced receiver scintillation data. *Journal of Geophysical Research*, *94*(A9), 11,959–11,969.

Bhattacharyya, A., Groves, K., Basu, S., Kuenzler, H., Valladares, C., & Sheehan, R. (2003). L-band scintillation activity and space-time structure of low-latitude UHF scintillations. *Radio Science*, *38*, 1004. https://doi.org/10.1029/2002RS002711

Bhattacharyya, A., Kakad, B., Gurram, P., Sripathi, S., & Sunda, S. (2017). Development of intermediate-scale structure at different altitudes within an equatorial plasma bubble: Implications for L-band scintillations. *Journal of Geophysical Research: Space Physics*, *122*, 1015–1030. https://doi.org/10.1002/2016JA023478

Bhattacharyya, A., & Yeh, K. (1988). Intensity correlation function for waves of different frequencies propagating through a random medium. *Radio science*, *23*(05), 791–808.

Blanc, M., & Richmond, A. (1980). The ionospheric disturbance dynamo. *Journal of Geophysical Research*, *85*(A4), 1669–1686. https://doi.org/10.1029/JA085iA04p01669

Briggs, B. H. (1984). *The analysis of spaced sensor records by correlation techniques: Middle atmosphere program*, Handbook for MAP, (Vol. 13, pp. 166–186). United States: In International Council of Scientific Unions Middle Atmosphere Program.

Burke, W. J., Gentile, L. C., Huang, C. Y., Valladares, C. E., & Su, S. Y. (2004). Longitudinal variability of equatorial plasma bubbles observed by DMSP and ROCSAT-1. *Journal of Geophysical Research*, *109*, A12301. https://doi.org/10.1029/2004JA010583

Chakrabarty, D., Fejer, B., Gurubaran, S., Pant, T. K., Abdu, M., & Sekar, R. (2014). On the pre-midnight ascent of F-layer in the June solstice during the deep solar minimum in 2008 over the Indian sector. *Journal of Atmospheric and Solar-Terrestrial Physics*, *121*, 177–187.

Costa, E., & Basu, S. (2002). A radio wave scattering algorithm and irregularity model for scintillation predictions. *Radio Science*, *37*(3), 1046.

Engavale, B., & Bhattacharyya, A. (2005). Spatial correlation function of intensity variations in the ground scintillation pattern produced by equatorial spread-F irregularities. *Indian Journal of Radio and Space Physics*, *34*(1), 23.

Engavale, B., Jeeva, K., Nair, K. U., & Bhattacharyya, A. (2005). Solar flux dependence of coherence scales in scintillation patterns produced by ESF irregularities. *Annales Geophysicae*, *23*(10), 3261–3266. https://doi.org/10.5194/angeo-23-3261-2005

Fejer, B. G., Jensen, J. W., & Su, S.-Y. (2008). Seasonal and longitudinal dependence of equatorial disturbance vertical plasma drifts. *Geophysical Research Letters*, *35*, L20106.

Fejer, B. G., & Scherliess, L. (1997). Empirical models of storm time equatorial zonal electric fields. *Journal of Geophysical Research*, *102*(A11), 24,047–24,056. https://doi.org/10.1029/97JA02164

Huang, C. M. (2013). Disturbance dynamo electric fields in response to geomagnetic storms occurring at different universal times. *Journal of Geophysical Research: Space Physics*, *118*, 496–501. https://doi.org/10.1029/2012JA018118

Huang, C.-S., & Kelley, M. C. (1996). Nonlinear evolution of equatorial spread F: 1. On the role of plasma instabilities and spatial resonance associated with gravity wave seeding. *Journal of Geophysical Research*, *101*(A1), 283–292.

Huang, C.-M., Richmond, A., & Chen, M.-Q. (2005). Theoretical effects of geomagnetic activity on low-latitude ionospheric electric fields. *Journal of Geophysical Research*, *110*, A05312. https://doi.org/10.1029/2004JA010994

Hysell, D., Kelley, M., Swartz, W., & Woodman, R. (1990). Seeding and layering of equatorial spread F by gravity waves. *Journal of Geophysical Research*, *95*(A10), 17,253–17,260.

Joshi, L. M., Balwada, S., Pant, T., & Sumod, S. (2015). Investigation on F layer height rise and equatorial spread F onset time: Signature of standing large-scale wave. *Space Weather*, *13*(4), 211–219. https://doi.org/10.1002/2014SW001129

Kakad, B., Gurram, P., Tripura Sundari, P. N. B., & Bhattacharyya, A. (2016). Structuring of intermediate scale equatorial spread F irregularities during intense geomagnetic storm of solar cycle 24. *Journal of Geophysical Research: Space Physics*, *121*, 7001–7012. https://doi.org/10.1002/2016JA022635

Kakad, B., Jeeva, K., Nair, K. U., & Bhattacharyya, A. (2007). Magnetic activity linked generation of nighttime equatorial spread F irregularities. *Journal of Geophysical Research*, *112*, A07311. https://doi.org/10.1029/2006JA012021

Kakad, B., Nayak, C. K., & Bhattacharyya, A. (2012). Power spectral characteristics of ESF irregularities during magnetically quiet and disturbed days. *Journal of Atmospheric and Solar-Terrestrial Physics*, *81–82*, 41–49. https://doi.org/10.1016/j.jastp.2012.04.008

Kakad, B., Surve, G., Tiwari, P., Yadav, V., & Bhattacharyya, A. (2017). Disturbance dynamo effects over low-latitude F region: A study by network of VHF spaced receivers. *Journal of Geophysical Research: Space Physics*, *122*, 5670–5686. https://doi.org/10.1002/2016JA023498

Kakad, B., Tiwari, D., & Pant, T. (2011). Study of disturbance dynamo effects at nighttime equatorial F region in Indian longitude. *Journal of Geophysical Research*, *116*, A12318. https://doi.org/10.1029/2011JA016626

Kakad, B., Tiwari, D., & Pant, T. (2012). Study of post sunset vertical plasma drift at equatorial F-region using long-term (1990–2003) ionosonde measurements in Indian longitude. *Journal of Atmospheric and Solar-Terrestrial Physics*, *80*, 239–246.

Kelley, M. C., Baker, K., & Ulwick, J. (1979). Late time barium cloud striations and their possible relationship to equatorial spread F. *Journal of Geophysical Research*, *84*(A5), 1898–1904.

Kelley, M., Larsen, M., LaHoz, C., & McClure, J. (1981). Gravity wave initiation of equatorial spread F: A case study. *Journal of Geophysical Research*, *86*(A11), 9087–9100.

Keskinen, M., Ossakow, S., Fejer, B. G., & Emmert, J. (2006). Evolution of equatorial ionospheric bubbles during a large auroral electrojet index increase in the recovery phase of a magnetic storm. *Journal of Geophysical Research*, *111*, A02303. https://doi.org/10.1029/2005JA011352

Kikuchi, T., Hashimoto, K. K., & Nozaki, K. (2008). Penetration of magnetospheric electric fields to the equator during a geomagnetic storm. *Journal of Geophysical Research*, *113*, A06214. https://doi.org/10.1029/2007JA012628

Kikuchi, T., Lhr, H., Schlegel, K., Tachihara, H., Shinohara, M., & Kitamura, T.-I. (2000). Penetration of auroral electric fields to the equator during a substorm. *Journal of Geophysical Research*, *105*(A10), 23,251–23,261. https://doi.org/10.1029/2000JA900016

Krall, J., Huba, J., & Fritts, D. (2013). On the seeding of equatorial spread F by gravity waves. *Geophysical Research Letters*, *40*, 661–664. https://doi.org/10.1002/grl.50144

Ledvina, B., Kintner, P., & de Paula, E. (2004). Understanding spaced-receiver zonal velocity estimation. *Journal of Geophysical Research*, *109*, A10306. https://doi.org/10.1029/2004JA010489

Li, G., Ning, B., Hu, L., Liu, L., Yue, X., Wan, W., et al. (2010). Longitudinal development of low-latitude ionospheric irregularities during the geomagnetic storms of July 2004. *Journal of Geophysical Research*, *115*, A04304. https://doi.org/10.1029/2009JA014830

Li, G., Ning, B., Liu, L., Zhao, B., Yue, X., Su, S.-Y., et al. (2008). Correlative study of plasma bubbles, evening equatorial ionization anomaly, and equatorial prereversal E× B drifts at solar maximum. *Radio Science*, *43*, RS4005. https://doi.org/10.1029/2007RS003760

Manoj, C., & Maus, S. (2012). A real-time forecast service for the ionospheric equatorial zonal electric field. *Space Weather*, *10*, S09002. https://doi.org/10.1029/2012SW000825

Maruyama, N., Richmond, A. D., Fuller-Rowell, T. J., Codrescu, M. V., Sazykin, S., Toffoletto, F. R., et al. (2005). Interaction between direct penetration and disturbance dynamo electric fields in the storm-time equatorial ionosphere. *Geophysical Research Letters*, *32*, L17105. https://doi.org/10.1029/2005GL023763

Maruyama, T., Saito, S., Kawamura, M., & Nozaki, K. (2008). Thermospheric meridional winds as deduced from ionosonde chain at low and equatorial latitudes and their connection with midnight temperature maximum. *Journal of Geophysical Research*, *113*, A09316. https://doi.org/10.1029/2008JA013031

Niranjan, K., Brahmanandam, P., Rao, P. R., Uma, G., Prasad, D., & Rao, P. R. (2003). Post midnight spread-F occurrence over Waltair (17.7N, 83.3E) during low and ascending phases of solar activity, *21* (pp. 745–750).

Nishioka, M., Saito, A., & Tsugawa, T. (2008). Occurrence characteristics of plasma bubble derived from global ground-based GPS receiver networks. *Journal of Geophysical Research*, *113*, A05301. https://doi.org/10.1029/2007JA012605

Patra, A., Rao, P., Anandan, V., & Jain, A. (1997). Radar observations of 2.8 m equatorial spread-F irregularities. *Journal of Atmospheric and Solar-Terrestrial Physics*, *59*(13), 1633–1641.

Richmond, A., Peymirat, C., & Roble, R. (2003). Long-lasting disturbances in the equatorial ionospheric electric field simulated with a coupled magnetosphere-ionosphere-thermosphere model. *Journal of Geophysical Research*, *108*(A3), 1118. https://doi.org/10.1029/2002JA009758

Sahai, Y., Fagundes, P., & Bittencourt, J. (2000). Transequatorial F-region ionospheric plasma bubbles: Solar cycle effects. *Journal of Atmospheric and Solar-Terrestrial Physics*, *62*(15), 1377–1383.

Sastri, J. H. (1999). Post-midnight onset of spread-F at Kodaikanal during the June solstice of solar minimum. *Annales Geophysicae*, *17*(8), 1111–1115. https://doi.org/10.1007/s00585-999-1111-4

Sekar, R., Suhasini, R., & Raghavarao, R. (1995). Evolution of plasma bubbles in the equatorial F region with different seeding conditions. *Geophysical Research Letters*, *22*(8), 885–888.

Smith, J., & Heelis, R. A. (2017). Equatorial plasma bubbles: Variations of occurrence and spatial scale in local time, longitude, season, and solar activity. *Journal of Geophysical Research: Space Physics*, *122*, 5743–5755. https://doi.org/10.1002/2017JA024128

Smith, J. M., Rodrigues, F. S., Fejer, B. G., & Milla, M. A. (2016). Coherent and incoherent scatter radar study of the climatology and day-to-day variability of mean F region vertical drifts and equatorial spread F. *Journal of Geophysical Research: Space Physics*, *121*, 1466–1482. https://doi.org/10.1002/2015JA021934

Sripathi, S. (2017). A seasonal study on the role of h'F/meridional winds in influencing the development of ESF irregularities over Indian sector. *Advances in Space Research*, *60*, 652–666.

Sripathi, S., Kakad, B., & Bhattacharyya, A. (2011). Study of equinoctial asymmetry in the equatorial spread F (ESF) irregularities over Indian region using multi-instrument observations in the descending phase of solar cycle 23. *Journal of Geophysical Research*, *116*, A11302. https://doi.org/10.1029/2011JA016625

Tiwari, D., Engavale, B., Bhattacharyya, A., Devasia, C., Pant, T., & Sridharan, R (2006). Simultaneous radar and spaced receiver VHF scintillation observations of ESF irregularities.

Tsunoda, R. T. (1985). Control of the seasonal and longitudinal occurrence of equatorial scintillations by the longitudinal gradient in integrated E region Pedersen conductivity. *Journal of Geophysical Research*, *90*(A1), 447–456. https://doi.org/10.1029/JA090iA01p00447

Tsunoda, R. T. (2012). A simple model to relate ionogram signatures to large-scale wave structure. *Geophysical Research Letters*, *39*, L18107. https://doi.org/10.1029/2012GL053179

Valladares, C., Sheehan, R., Basu, S., Kuenzler, H., & Espinoza, J. (1996). The multi-instrumented studies of equatorial thermosphere aeronomy scintillation system: Climatology of zonal drifts. *Journal of Geophysical Research*, *101*(A12), 26,839–26,850.

Yeh, K. C., & Liu, C.-H. (1982). Radio wave scintillations in the ionosphere. *Proceedings of the IEEE*, *70*(4), 324–360.

Yokoyama, T. (2017). A review on the numerical simulation of equatorial plasma bubbles toward scintillation evaluation and forecasting. *Progress in Earth and Planetary Science*, *4*(1), 37.